HEAT TRANSFER AND FLUID FLOW MODEL ASSISTED MECHANICAL ANALYSIS FOR WIRE ARC DIRECTED ENERGY DEPOSITION TO IMPROVE RESIDUAL STRESS AND DISTORTION PREDICTION

P. K. DILJITH*[1], ARYAN**, W. ZHANG**, A. DE*

**Mechanical Engineering Department, Indian Institute of Technology Bombay, 400076, Mumbai, India*
Orcid Id:0000-0001-9522-7838, 0000-0002-3109-261X
***Department of Materials Science and Engineering, The Ohio State University, 43221, Ohio, USA*
Orcid Id:0000-0002-7570-0488, 0000-0003-4543-2563

DOI 10.3217/978-3-99161-089-2-024, license CC BY 4.0

ABSTRACT

A substantive design of process variables and scanning strategy in wire arc directed energy deposition (DED-Arc) requires an estimation of the thermal distortion and residual stress. Routine sequential heat transfer and thermomechanical stress analyses neglect the convective heat transport in the melt pool that commonly affects the computational accuracy. We propose here to compute the deposit profile and temperature field using a finite volume-based heat transfer and fluid flow model and use the computed temperature field for a subsequent mechanical analysis. The computed melt pool profile, deposition profile and residual stress showed a maximum discrepancy of around 10% against experimentally measured results for single- and multi-track DED-Arc depositions. An assessment of the increased computational demand vis-à-vis enhanced prediction accuracy due to the integration of a heat transfer and fluid flow model over a heat conduction only model is presented. Further efforts to simulate multi-track multi-layer DED-Arc using the proposed approach are underway.

Keywords: Wire arc directed energy deposition, Heat transfer and fluid flow model, Thermomechanical analysis, Residual stress and distortion, Computational accuracy.

INTRODUCTION

Wire arc directed energy deposition (DED-Arc) is a layer-by-layer additive manufacturing process that uses an electric arc to melt a filler wire, which solidifies to form three-dimensional components [1-2]. DED-Arc has attracted a significant interest due to low cost of filler wire feedstock in comparison to metallic powder [3] and a high deposition rate almost up to 4 kg/h [4]. However, high residual stress [5] and distortion [6] of the deposited part has remained a critical challenge for the DED-Arc built parts. A prior quantitative estimation of the temperature field, and thermomechanical residual stress and distortion is becoming increasingly important in design for DED-Arc process [7]. With the growth of computational capacity and efficiency, high fidelity models are increasingly used to help design DED-Arc process [8].

Sequentially coupled heat conduction and thermomechanical stress analyses are used to simulate the temperature field, and the residual stress and distortion for DED-Arc of small to medium size builds [9-10]. Conventional thermo-mechanical methods based on heat conduction analysis require a pre-defined build profile, which is routinely considered as a simple shape [11-12] or obtained from an experimentally measured deposit [13-14] thereby limiting the model capability. These models also require considering complex heat source configurations such as hemispherical Gaussian [11], double-ellipsoid [15-16], circular surface [17], and conical [18-19]. The pre-defined deposit profile is introduced during the modelling calculations in an artificial manner [20-21]. A physics-based heat transfer model that captures the evolution of melt pool profile and deposit dimensions in a mechanistic manner can minimize errors from assumed geometries and heat sources, ensuring accurate prediction of distortion and residual stress.

To address these limitations, research has focused on incorporating convective flow and integrating thermal-fluid models with mechanical models. Heat transfer and fluid flow models account for convective flows by solving the conservation equations for mass, momentum, and energy. Mukherjee et al. [22] reported a 3D transient heat transfer and fluid flow coupled mechanical analysis for the prediction of residual stress in DED-Arc of simplified geometry. Chen et al. [23] reported a similar coupled thermo-fluid and mechanical analysis for laser powder bed fusion (LPBF) process. Bailey et al. [24] simulated the deposition of three single layers using a coupled fluid flow model and mechanical analysis for the prediction of residual stress. Gao et al. [25] also reported a similar coupled thermo-fluid and mechanical analysis for layer-by-layer deposition. The aforementioned studies reported the challenges of high computational demands and could handle the simulation of either a few tracks or a few layers. Furthermore, despite these advancements, geometric simplifications remain prevalent, and most studies are restricted to simple geometries.

This study presents a high-fidelity modelling approach to compute residual stress and distortion in DED-Arc fabricated components. The framework integrates a thermal-fluid flow model that captures the melting physics of filler wire to generate the temperature distribution and realistic deposition profile, which is then mapped to a mechanical model. The volume of fluid approach in the thermo-fluid analysis eliminates the need to assume an artificial bead profile enabling enhanced predictability and adaptability. In the mechanical model, the elements are activated based on their thermal history using a subroutine that assigns a valid

volume fraction. The computed results are validated against experimentally measured values from independent literature and compared with a conventional heat-conduction-based thermomechanical model. This comprehensive approach will prove essential for a more informed prior assessment of the structural integrity and dimensional consistency of DED-Arc fabricated parts.

NUMERICAL MODELLING

HEAT TRANSFER AND FLUID FLOW MODEL

In this work, a finite element volume-based heat transfer and fluid flow model is used to simulate the transient temperature field and material flow for single- and multi-layer DED-Arc process. The solution domain embodies both the substrate and the filler wire. The following assumptions are considered for the modelling calculations. The molten metal flow within the melt pool is assumed to be laminar and incompressible. The effect of shielding gas and the evaporation of alloying elements are neglected [22,26]. The effects of arc pressure [27] and Lorentz forces [28] are omitted, as their influence is negligible at currents below 250 A and for relatively smaller melt pools in DED-Arc in comparison to arc welding.

The arc plasma heat transfer and fluid flow is not directly considered in the simulation. Instead, the current model follows the standard method to represent the effect of arc plasma by applying a surface heat flux in the form of a Gaussian distribution. Such heat flux distribution is described by two parameters: the arc radius and the heat source efficiency. The arc radius is assumed to have a constant value of 1.5 mm based on the literature data for GMAW-based WAAM processes. For the heat source efficiency, the initial values in the range of 0.70 to 0.85 were selected based on the literature data. The value was then adjusted only for the first deposited layer to obtain agreement with experimentally observed bead geometry. For multilayer simulations, the same efficiency value was retained for all subsequent layers, and no further adjustment was applied.

For simplicity, the current model also does not directly consider the filler metal transfer. The addition of filler metal into the melt pool is represented by applying an equivalent mass flux to the melt pool surface.

The following governing equations of conservation of mass, momentum, and energy are solved.

$$\nabla \cdot (\rho\, \vec{v}) = 0 \tag{1}$$

$$\frac{\partial}{\partial t}(\rho\, \vec{v}) + \nabla \cdot (\rho\, \vec{v} \otimes \vec{v}) = \nabla \cdot (\mu \nabla\, \vec{v}) - \nabla P + \rho \vec{g} \tag{2}$$

$$\frac{\partial}{\partial t}(\rho h) + \nabla \cdot (\rho \vec{v} h) = \nabla \cdot (k \nabla T) \tag{3}$$

where $\vec{v}$ and $\vec{g}$ denote the velocity vector and gravitational acceleration vector, respectively, ρ is the density, μ is the viscosity, P is the pressure, k is the thermal conductivity, and T is the temperature. In Eq. (3), h *is the specific enthalpy that is defined as* $h = \int C(T)dT + (1 - f_s)L$, where $C(T)$, L and f_s are the specific heat, latent heat of melting, and fraction of the solid, respectively.

The deposit profile is modelled using the volume of fluid (VOF) method with each cell of a discretized mesh assigned to a time-dependent fluid fraction function. The function with a value of 1 represents the fluid region (comprising liquid and/or solid metal), 0 represents the non-fluid region, and a value in between 0 and 1 represents the interface containing the free surface, which is governed by partial derivatives in the form of Eq. (4) and solved to track the free surface of the molten pool.

$$\frac{\partial f_l}{\partial t} + \nabla \cdot (\vec{v}\ f_l) = 0 \tag{4}$$

where f_l denotes the fluid volume fraction in a cell, with f_l = 1 representing a cell fully occupied by fluid and f_l = 0 representing a void or gas region, and $\vec{v}$ is the velocity vector. Heat loss due to convection is considered on the deposit and substrate surfaces. Further detailed methodology for the heat transfer and fluid flow analysis is already reported in literature [29] and not repeated here.

MAPPING OF DEPOSITION PROFILE AND TEMPERATURE DISTRIBUTION

The model integrates the deposition profile and transient temperature field from the heat transfer and fluid flow model into the mechanical simulation. The overall mapping framework is illustrated in Fig. 1. The deposition profile is exported in a tessellated format (stl) from the thermal-fluid simulation. To ensure compatibility with the mechanical model, the stl file is curated to eliminate defects such as non-manifold edges, holes, inverted normal, and self-intersecting faces [30]. The geometry is imported to a commercial finite element method software (ABAQUS ver-2021) environment. A custom plugin is used to reconstruct the deposition geometry from the tessellated data [31].

Following the creation of the deposit geometry in ABAQUS, the domain is partitioned and discretized using three-dimensional tetrahedral elements with displacement degrees of freedom. Tetrahedral meshing is selected to accommodate the complex geometrical features of the deposited material [32], with finer meshes applied in the deposition region to accurately simulate element activation during the build process. Nodal coordinates are extracted, and transient temperature values are mapped from the CFD simulation at predefined time intervals. These temperature values are then applied as predefined boundary conditions in mechanical analysis, enabling coupled thermo-mechanical simulation, as shown in Fig. 1.

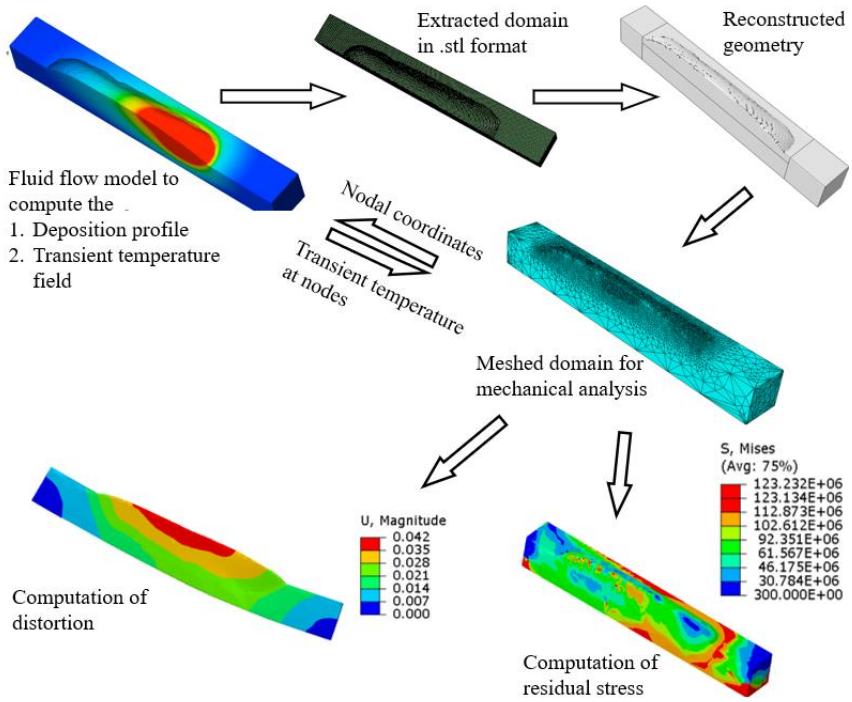

Fig. 1 Flowchart for the mapping of deposition profile and temperature distribution from CFD model to mechanical model

MECHANICAL MODEL

From the time varying pre-defined temperature field obtained from the fluid flow model, the displacement field in the mapped solution domain is calculated by solving the force equilibrium equation given by

$$[\mathrm{K}]\{\delta\} - \{f\} = 0 \tag{5}$$

where [K] is the global stiffness matrix, $\{\delta\}$ is the unknown nodal displacement vector at all the nodes of the solution domain and $\{f\}$ embodies the contribution from the thermal strain induced body force from all the elements. Eq. (5) is solved for $\{\delta\}$ considering the structural boundary conditions and for a given temperature gradient between two successive time steps. The nonlinearity due to plasticity is incorporated by defining Von Mises yield criterion and solving for displacement using the Prandtl-Reuss flow rule. The resultant displacement is a sum of elastic, plastic and thermal displacements as shown in Eq. 6. The volumetric strain due to solid-state phase transformation is considered negligible for the selected alloys, AA5356 and austenitic stainless steel, used for the model calculations [33,34].

$$\varepsilon_{total} = \varepsilon_{elastic} + \varepsilon_{plastic} + \varepsilon_{thermal} \quad (6)$$

To model the experimental clamping conditions, all the nodes in the respective positions are restricted in the x, y, and z directions. The boundary condition is given by the Eq. 7.

$$U_x = U_y = U_z = 0 \quad (7)$$

The simulation of material deposition in the mechanical analysis is carried out using an approach that alters the volume fraction of the element. Initially, the elements representing the deposited track are assigned a volume fraction of zero. In the following steps, the elements that obtain an average temperature that equals the melting point of the material is assigned a volume fraction of one using an Abaqus subroutine UEPACTIVATIONVOL.

MODEL TESTING AND VALIDATION

APPLICATION OF INTEGRATED MODEL TO SINGLE-TRACK SINGLE-LAYER DEPOSITION MODEL

The present model is demonstrated for a simple single-track, single-layer DED-Arc deposition of AA5356. The process is performed at a printing travel speed of 30 mm/s and an arc power of around 1.6 kW. The chemical composition of the material and their temperature dependent material properties are obtained from the literature [35].

To understand the importance of liquid metal convection over conduction on heat transfer, the Peclet number is estimated which is defined as $Pe = L\,u/\alpha$, where L is the characteristic length (e.g., pool width), u is the representative fluid velocity, and α is the thermal diffusivity. The results calculated by the heat transfer and fluid flow model for the AA5356 melt pool show u = 0.3 m/s and L = 0.006 m, resulting in a Peclet number of ~30. As this value is much larger than 1, the convective heat transport within the melt pool is considered significant for this case.

The transient temperature field computed by the heat transfer and fluid flow model is mapped into the mechanical model. The melt pool profile obtained by the temperature field mapping in the mechanical model is shown at three different locations along the deposition length in Fig. 2 (a-c). The profile simulated by the heat transfer and fluid flow model predicts a layer width of 3.5 mm, a layer height of 2.17 mm, and a penetration depth of 2.66 mm, as illustrated in Fig. 2 (d), confirming that the transient temperature field is transferred to the mechanical model with a satisfactory accuracy. Some distortion in the smoothness of the deposit profile arises from the tetrahedral meshing used to capture the geometry. A comparison between the deposition profile obtained from the fluid flow model and that mapped into the mechanical model is presented in Fig. 2 (e). Minor deviations are observed, which can be attributed to the unavoidable errors due to mapping. Nevertheless, the results show that both the deposition profile and temperature field are transferred from the fluid flow model to the mechanical model with a reasonable fidelity.

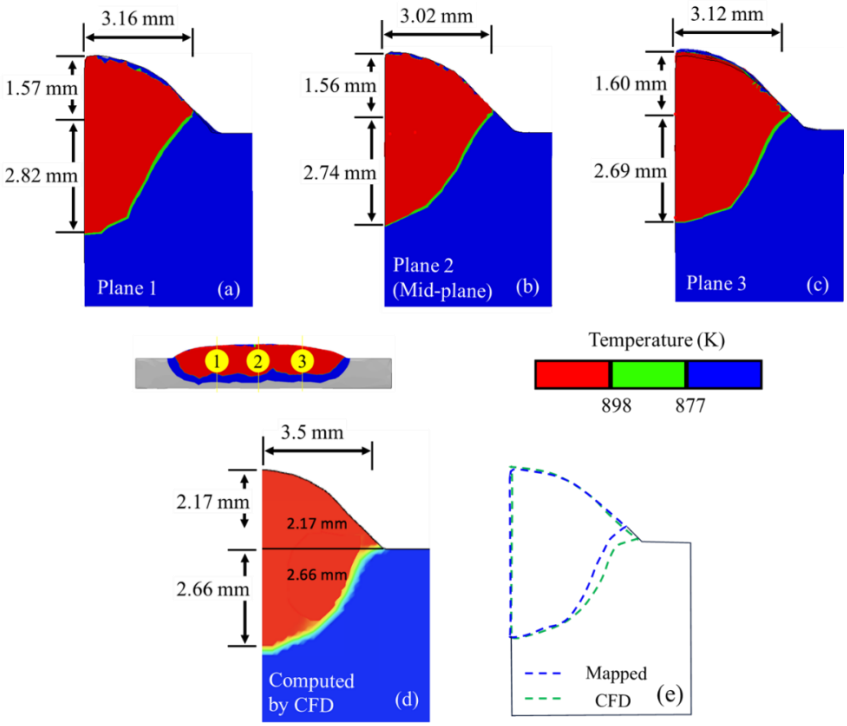

Fig. 2 Deposit profile in the mechanical model at three planes, (a) plane 1, (b) plane 2 (mid-plane) and (c) plane 3, along the longitudinal direction., (d) Computed deposit shape and melt pool profile using the fluid flow model, and (e) A comparison of the predicted deposit profile using the fluid flow model and that used for the mechanical analysis after mapping.

In contrast to conventional models, where elements are activated using a bounding box or choosing a pre-defined set of elements, synchronized with deposition speed, the present approach employs a subroutine-driven activation method based on the volume fraction technique. Fig. 3 compares the evolving deposition geometry predicted by the fluid flow model with that obtained through the element activation in the mechanical model at different time steps of the simulation. The results demonstrate that the subroutine successfully replicates the advancing deposition profile, with element activation closely matching the fluid flow prediction. Minor discrepancies in the profile topology can be attributed to the relatively coarse mesh and the larger time intervals selected to map the thermal field into the mechanical model. Nevertheless, the isotherms within the deposited region confirm that the temperature distribution is accurately mapped from the fluid flow analysis to the mechanical model.

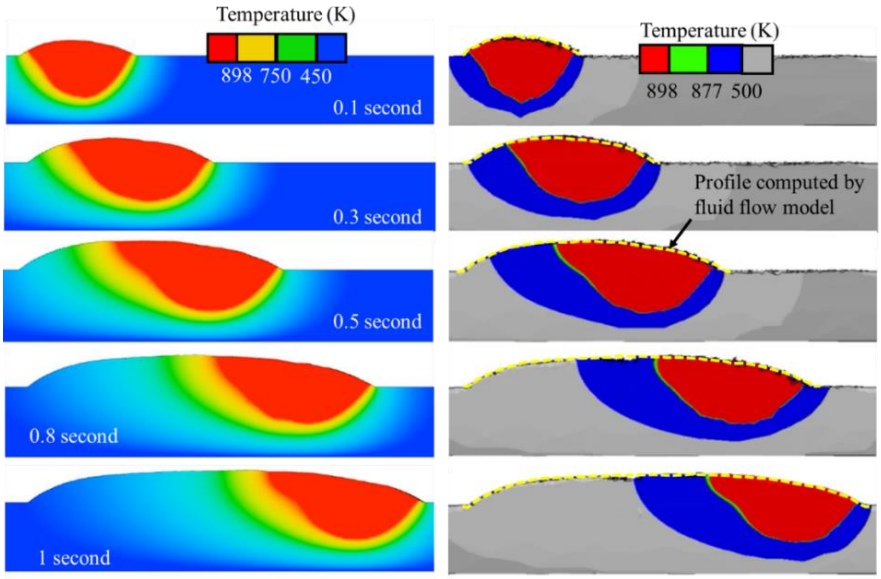

Fig. 3 The comparison of the deposit profile computed by the fluid flow model and that activated in the mechanical model, using the subroutine, at different time instances in the mechanical analysis. The section presented in the figure is the mid plane in the transverse axis (Y-axis).

Fig. 4 presents the boundary condition (BC) applied and the mechanical results computed by the mechanical model. Taking advantage of the symmetry, the half of the deposited profile computed by the fluid flow model is imported to the mechanical analysis. Fig. 4 (a) presents the symmetrical BC applied along the plane of symmetry [36] and the clamping conditions applied by restricting the displacement of the corresponding nodes along all the directions. After the deposition, the nodes under the clamping BC are released and simple boundary conditions are applied [33]. The longitudinal residual stress along the line 1 is presented in Fig. 4 (b). The model can accurately predict the development of residual stress near the deposition line due to the shrinkage of the molten pool and compensatory stresses away from the deposition centreline [37-38]. The peak magnitude of the tensile and compressive residual stresses, 150 MPa and 75 MPa, are comparable to the stresses reported in the literature [33]. The nature of stress in Fig. 4(b) exhibits a sharp gradient at the centreline (y=0). Theoretically, the slope should be zero due to symmetry. The observed sharpness is attributed to a numerical artifact arising from the tetrahedral mesh at the symmetry boundary.

Fig. 5 (c) illustrates the transverse residual stress predicted by the mechanical model along the line 1, where the magnitude of the transverse stress is significantly lower than the longitudinal residual stress due to the reduced constraint in the transverse direction [39-40]. Near the deposition centreline, the transverse stress exhibits both tensile and compressive values, ranging from 44 MPa tensile to 31 MPa compressive, arising from the contraction and expansion of the metal during solidification, while the regions farther from the centreline approach zero, consistent with observations in the literature [12,40]. Fig. 4 (d) presents the

distortion in the build direction along a line at the bottom of the substrate in the longitudinal direction, where the predicted distortion pattern agrees with previously reported results [12,33]. The relatively low distortion magnitude may be attributed to the short deposition length [12], whereas the asymmetry in the distortion profile could result from the higher thermal gradient near the weld endpoint [41].

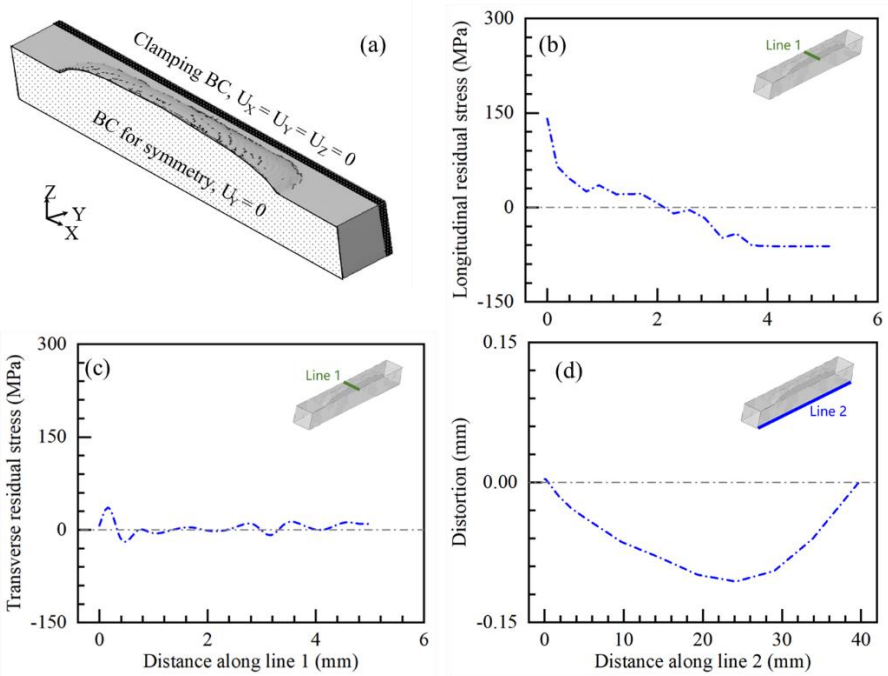

Fig. 4 (a) Boundary conditions used in mechanical modelling of single track single layer DED-Arc deposition. (b) Longitudinal and (c) transverse residual stress along Line 1 (d) Distortion in the Z direction along the line 2.

APPLICATION OF INTEGRATED MODEL TO SINGLE-TRACK MULTI-LAYER DEPOSITION

The model is next applied to a single-track, five-layer DED-Arc deposition of SS316L on SS304L and is validated against experimentally measured results reported in the literature [34]. The deposition is carried out at a wire feed rate (WFR) of 3.3 m/min and a printing travel speed (PTS) of 7 mm/s with the first layer being deposited at a slightly higher WFR of 4.2 m/min to ensure proper wetting. A bidirectional deposition strategy with an interlayer dwell time of 35 seconds is employed. Temperature dependent thermophysical properties are employed in the model [42].

The Peclet number for the SS316L melt pool is estimated using the calculation results from the heat transfer and fluid flow model. Given that u = 0.2 m/s and L = 0.006 m, the Peclet number is found to be ~200, indicating that the liquid metal convection plays a critical role in heat transport within the SS316L melt pool. This number is even higher than that for the AA5356 melt pool reported previously which is due to the factor that the stainless steel has much lower thermal diffusivity than the aluminium alloy.

Fig. 5 illustrates the progressive layer-wise melt pool evolution during the single-track five-layer deposition, highlighting the liquidus and solidus isotherms for each layer. In layer 1, as shown in Fig. 5 (a), the melt pool penetrates the substrate, ensuring metallurgical bonding and providing a strong foundation for subsequent layers. The increase in bead width due to higher WFR is also evident in the figure. As additional layers are deposited, the melt pool grows larger and shifts upward, with the overlapping heat-affected zones visible across the adjacent layers. The thermal field demonstrates reheating of underlying material, leading to partial remelting and thermal cycling, as shown in Fig. 5 (b-e). A comparison of computed melt pool profiles with experimentally measured macrograph in Fig. 5 (f) confirms a good agreement in the bead shape and layer buildup. Overall, Fig. 5 shows that the model can fairly predict the melt pool geometry and interlayer fusion for DED-Arc.

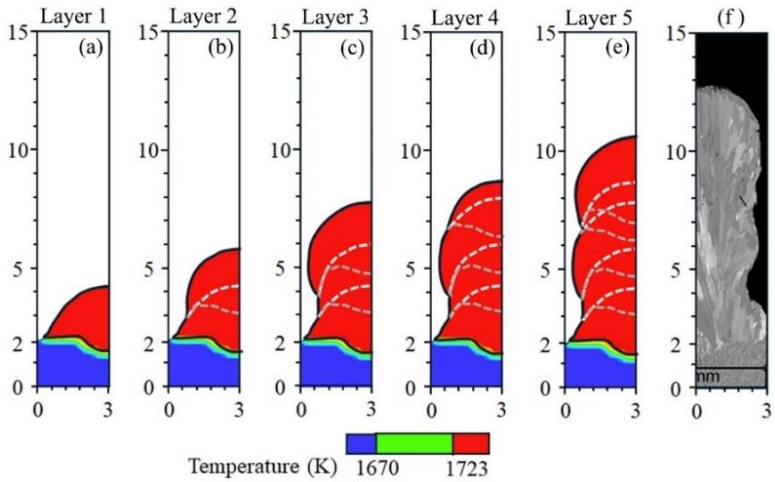

Fig. 5 Melt pool profile for layers (a-e) one to five in a single-track five-layer deposition and its comparison with (f) experimentally measured macrograph [34]

Fig. 6 presents a comparison of the computed and experimentally measured residual stress [34] for the single-track five-layer DED-Arc deposition. Fig. 6 (a) illustrates the boundary conditions applied in the mechanical model, where symmetry constraints are imposed along the central plane to reduce computational effort. The clamping boundary conditions are applied on the left end of the substrate, and the right end is left free to move as per the experimental conditions [34]. Fig. 6 (b) shows the longitudinal residual stress distribution along the line in the Z-axis at the mid-plane of the deposition length, highlighting differences

between computed and measured values. The computed stress follows a similar trend but slightly overpredicts the tensile stress magnitudes near the top region. Both curves capture the transition from the tensile to the compressive stress across the height. The agreement indicates that the model successfully represents the dominant thermomechanical behaviour despite localized discrepancies.

Fig. 6 (c) presents the normal residual stress along the Z-axis, where both computed and measured results oscillate around zero. The model captures the general fluctuations, though the amplitude shows little local deviations. Fig. 6 (d) shows a comparison between the computed and experimentally measured transverse residual stress distribution across the height. The overall stress magnitudes remain within ±200 MPa, and the computed results reasonably track the experimental fluctuations. Both datasets indicate alternating compressive and tensile zones, reflecting complex thermal contraction effects during solidification. The agreement in stress oscillations validates the robustness of the numerical approach. These results demonstrate that the model can effectively capture three-dimensional stress variations in multi-layer DED-Arc built components.

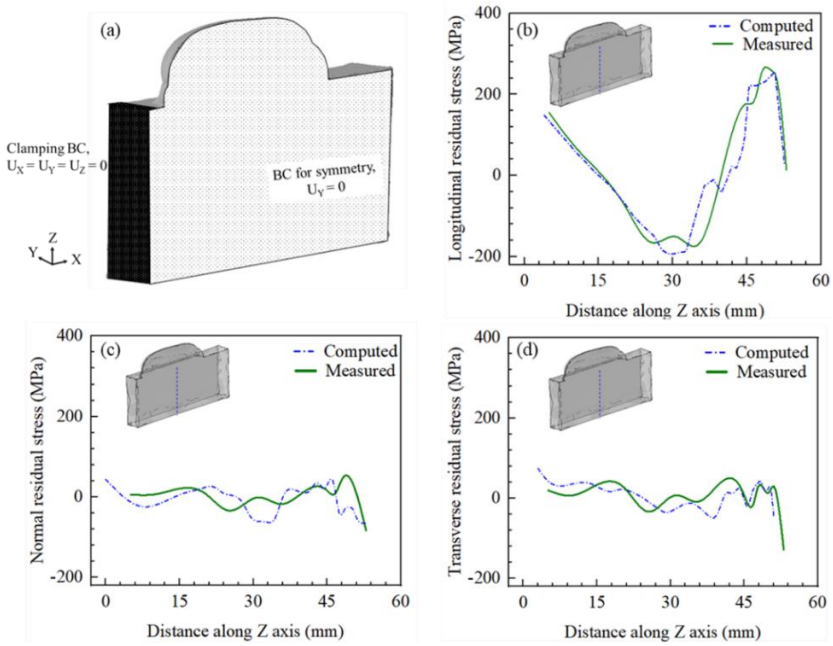

Fig. 6 (a) Boundary conditions used in mechanical modelling of single-track five-layer deposition. Comparison of computed (b) longitudinal (c) normal and (d) transverse residual stress with that measured by neutron diffraction [34] along the build direction.

COMPUTATIONAL SUBTILITIES

To compare with the conventional models, newer high-fidelity approaches require a systematic index to evaluate the trade-off between the quality of computed results and the computational subtilities. Models can therefore be differentiated based on their computational requirements and predictive outputs. Important factors influencing this differentiation include accuracy, computational speed, the level of approximations, domain size, the extent of user intervention, and data storage overhead [43-44]. These requirements determine whether a modelling approach is better suited for feasibility studies, process optimization, or detailed validation tasks. Table 1 shows the computational subtilities of a conventional sequentially coupled thermomechanical approach for modelling residual stress and distortion for two single-track multi-layer cases reported in the literature [45]. A single-track twenty-layer deposition of aluminium alloy (case 1) and a single-track four-layer part scale deposition of steel alloy (case 2) is compared with the current approach.

The comparison clearly demonstrates that while conventional thermomechanical approaches provide relatively lower computational costs, they sacrifice accuracy and remain heavily dependent on user intervention. Case 1, with 78.30% accuracy and the longest runtime of 47.72 hours, highlights the inefficiency of simplified assumptions when applied to realistic deposition scenarios. Even though Case 2 improves accuracy to 86.28% and reduces the total runtime to 16.33 hours, it still relies on assumptions about deposition profiles and heat sources. Such reliance not only limits predictive fidelity but also introduces subjective dependencies during model preparation, which can affect repeatability of the computed results. Both cases involve significant manual effort in defining the deposition strategies and heat sources, which undermines their robustness in industrial practice. Additionally, the simplified treatment of process physics restricts their applicability when higher fidelity is essential. Although they demand a modest computational storage, the trade-off comes at the expense of the prediction reliability.

In contrast, the heat transfer and fluid flow integrated thermomechanical model emerges as a relatively more preferable option despite its higher computational demands. With an accuracy of around 90% for the cases considered in the present work, it provides a more reliable representation of the underlying process physics, reducing reliance on assumptions and manual intervention. The mismatch between the computed and measured values falls well within the inherent uncertainty of a reliable model. Such deviations are expected due to the natural dispersion of temperature-dependent thermophysical properties (around 10% as reported in Touloukian's data) [46] along with minor variations in the alloy composition and routine experimental errors. Additional discrepancies also originate from model assumptions and simplified boundary conditions. On the other hand, the experimentally measured residual stress values are also likely to have inherent measurement uncertainty. Considering these unavoidable sources of uncertainty, the agreement achieved by the model can be regarded as fairly satisfactory.

Conversely, the higher predictive accuracy demands higher computation time and storage overhead. The thermal analysis is computationally intensive, but the total simulation time of 34.40 hours is still reasonable given the substantial gain in predictive capability. Furthermore, the model eliminates approximations, ensuring that process-induced stresses and distortions

are captured with greater confidence. While its storage overhead of 184.9 GB is higher, the modern computational resources and software can accommodate such requirements, especially when balanced against the benefits of accuracy and reduced trial-and-error in experiments. The streamlined assumptions, focusing only on material properties and boundary conditions, make the approach more generalizable across different deposition scenarios. Therefore, despite the higher resource consumption, the integrated model offers superior robustness and predictive reliability, making it the most suitable choice for advancing industrial-scale additive manufacturing simulations.

Table 1 Comparison of the fluid flow integrated mechanical model presented in this paper with conventional thermomechanical models of multi-layer DED-Arc deposits [45].

Computational subtility	**Conventional thermomechanical modelling – Case 1.**	**Conventional thermomechanical modelling – Case 2.**	**Heat transfer and fluid flow integrated thermomechanical model**
Accuracy of prediction	78.30%	86.28%	92.56%
Time for thermal analysis	0.61 hours	3.55 hours	30.24 hours
Time for mechanical analysis	46.62 hours	12.78 hours	4.16 hours
Total time	47.72 hours	16.33 hours	34.40 hours
Assumptions	Deposition profile, heat source, material properties, boundary conditions	Deposition profile, heat source, material properties, boundary conditions	Material properties, boundary conditions
User intervention	Creating the deposition profile, Designing the heat source, Pre-processing of the solution domain	Creating the deposition profile, Designing the heat source, Pre-processing of the solution domain	Pre-processing of the solution domain, Mapping the deposition profile, Mapping the temperature field.
Domain size	150 × 75 × 28 mm3	500 × 60 × 12 mm3	5.0 × 0.5 × 2. mm3
Data storage overhead	15.46 GB	8.95 GB	184.9 GB

CONCLUSIONS

A heat transfer and fluid flow model integrated thermomechanical analysis is reported here to compute deposition profile, melt pool dimensions, residual stress, and distortions in DED-Arc. The computed results are validated against experimentally measured results, demonstrating its robustness and applicability. The key findings of this work are summarized below:

- The integrated heat transfer and fluid flow–based approach achieves substantially higher accuracy (around 90%) compared to conventional conduction-based models (around 85%), enabling more reliable predictions of stress and distortion.
- By eliminating predefined deposition profiles and heat sources, the framework minimizes pre-processing subjectivity and improves repeatability. Furthermore, the use of UEPACTIVATIONVOL for element activation more faithfully captures the evolving deposition geometry than traditional block-type activation schemes.
- Although some manual input is still required for mapping and preprocessing, these steps can be streamlined in the future, reducing user intervention and improving efficiency.
- The model requires longer simulation time (34.4 h) and higher storage capacity (~185 GB) relative to conventional approaches. However, this is offset by the significant gain in predictive fidelity and the reduced need for experimental trial-and-error, making it increasingly viable with advances in computational power.

Comparing the effectiveness of integrated models requires comparison of not only accuracy but also computational speed, the level of approximations, domain size, the extent of user intervention, and data storage overhead. A unified index will be developed in the future to compare the different modelling approaches.

References

[1] P. K. CHAURASIA, B. K. BARIK, A. DAS, S. F. GOECKE, A. DE: 'Probing dimensional consistency during multi-track multi-layer gas metal arc directed energy deposition of aluminium alloys', *Weld World* 2024, 68:925-38.

[2] T. MUKHERJEE, J. S. ZUBACK, A. DE, T. DEBROY: 'Printability of alloys for additive manufacturing', *Sci Rep* 2016, 6:19717.

[3] S. W. WILLIAMS, F. MARTINA, A. C. ADDISON, J. DING, G. PARDAL, P. COLEGROVE: 'Wire + Arc Additive Manufacturing', *Mater Sci Technol* 2016, 32:641-7.

[4] H. STINSON, R. WARD, J. QUINN, C. MCGARRIGLE: 'Comparison of Properties and Bead Geometry in MIG and CMT Single Layer Samples for WAAM Applications', *Metals (Basel)* 2021, 11.

[5] Q. WU, T. MUKHERJEE, A. DE, T. DEBROY: 'Residual stresses in wire-arc additive manufacturing – Hierarchy of influential variables', *Addit. Manuf.* 2020, 35.

[6] Q. WU, T. MUKHERJEE, C. LIU, J. LU, T. DEBROY: 'Residual stresses and distortion in the patterned printing of titanium and nickel alloys', *Addit. Manuf.* 2019, 29.

[7] K. KHAN, L. S. MOHAN, A. DE, T. DEBROY: 'Rapid calculation of part scale residual stresses in powder bed additive manufacturing', *Sci. Technol. Weld. Join.*, vol. 28, 2023, p. 145-53.

[8] W. OU, G. L. KNAPP, T. MUKHERJEE, Y. WEI, T. DEBROY: 'An improved heat transfer and fluid flow model of wire-arc additive manufacturing', *Int. J. Heat Mass Transf.* 2021, 167:120835.

[9] M. KÖHLER, L. SUN, J. HENSEL, S. PALLASPURO, J. KÖMI, K. DILGER, Z. ZHANG: 'Comparative study of deposition patterns for DED-Arc additive manufacturing of Al-4046', *Mater. Des.*, 2021, 210:110122.

[10] H. ZHAO, C. GAO, Z. WANG, Q. WANG, C. LIU, Y. ZHAN: 'Residual stress analysis of TC4/Inconel718 functionally graded material produced by laser additive manufacturing based on progressive activation element method', *Int. J. Adv. Manuf. Technol.*, 2023, 129:1443-53.

[11] W. HUANG, Q. WANG, N. MA, H. KITANO: 'Distribution characteristics of residual stresses in typical wall and pipe components built by wire arc additive manufacturing', *J. Manuf. Process.*, 2022, 82:434-47.
[12] J. DING, P. COLEGROVE, J. MEHNEN, S. GANGULY, P. M. S. ALMEIDA, F. WANG, S. WILLIAMS: 'Thermo-mechanical analysis of Wire and Arc Additive Layer Manufacturing process on large multi-layer parts', *Comput. Mater. Sci.*, 2011, 50:3315-22.
[13] A. CHERGUI, N. BERAUD, F. VIGNAT, F. VILLENEUVE: 'Finite Element Modeling and Validation of Metal Deposition in Wire Arc Additive Manufacturing', In: L. Roucoules, M. Paredes, B. Eynard, P. Morer Camo, C. Rizzi, editors, Cham: *Springer International Publishing*, 2021, p. 61-6.
[14] K. P. PRAJADHIAMA, Y. H. MANURUNG, Z. MINGGU, F. H. PENGADAU, M. GRAF, A. HAELSIG, T. E. ADAMS, H. L. CHOO: 'Development of Bead Modelling for Distortion Analysis Induced by Wire Arc Additive Manufacturing using FEM and Experiment', *MATEC Web Conf* 2019, 269:05003.
[15] W. TANG, A. LIU, C. SONG, L. ZHOU: 'Numerical and experimental study of temperature, residual stresses, and microstructural evolution on multi-layer and multi-pass laser cladding of 6061Al alloy', *Mater. Res. Express*, 2024, 11:96512.
[16] K. OYAMA, S. DIPLAS, M. M'HAMDI, A. E. GUNNÆS, A. S. AZAR: 'Heat source management in wire-arc additive manufacturing process for Al-Mg and Al-Si alloys', *Addit. Manuf.*, 2019, 26:180-92.
[17] J. SUN, K. DILGER: 'Influence of preheating on residual stresses in ultra-high strength steel welded components', *J. Mater. Res. Technol.*, 2023, 25:3120-36.
[18] C. HEINZE, C. SCHWENK, M. RETHMEIER: 'Numerical calculation of residual stress development of multi-pass gas metal arc welding', *J. Constr. Steel Res.*, 2012, 72:12-9.
[19] G. AGARWAL, H. GAO, M. AMIRTHALINGAM, M. HERMANS: 'Study of solidification cracking susceptibility during laser welding in an advanced high strength automotive steel', *Metals (Basel)*, 2018, 8:673.
[20] X. F. ZHAO, A. WIMMER, M. F. ZAEH: 'Experimental and simulative investigation of welding sequences on thermally induced distortions in wire arc additive manufacturing', *Rapid Prototyp J.*, 2023, 29:53-63.
[21] D. ZHANG, D. DU, S. XUE, J. QI, Z. PU, Y. LU, Y. TANG, B. CHANG: 'Residual stress and deformation in wire-feed electron beam additive manufactured aluminum components', *Int. J. Adv. Manuf. Technol.*, 2024, 131:1665-76.
[22] T. MUKHERJEE, W. ZHANG, T. DEBROY: 'An improved prediction of residual stresses and distortion in additive manufacturing', *Comput. Mater. Sci.*, 2017, 126:360-72.
[23] F. CHEN, W. YAN: 'High-fidelity modelling of thermal stress for additive manufacturing by linking thermal-fluid and mechanical models', *Mater. Des.* 2020, 196:109185.
[24] N. S. BAILEY, C. KATINAS, Y. C. SHIN: 'Laser direct deposition of AISI H13 tool steel powder with numerical modeling of solid phase transformation, hardness, and residual stresses', *J. Mater. Process Technol.*, 2017, 247:223-33.
[25] M. Z. GAO, B. MONDAL, T. A. PALMER, W. ZHANG, T. DEBROY: 'Integrated modeling of cracking during deep penetration laser welding of nickel alloys', *Sci. Technol. Weld. Join.*, 2023, 28:689-700.
[26] V. MANVATKAR, A. DE, T. DEBROY: 'Heat transfer and material flow during laser assisted multi-layer additive manufacturing', *J. Appl. Phys.*, 2014, 116:124905.
[27] M. L. UN, T. W. EAGAR: *Influence of arc pressure on weld pool geometry*, 1985.
[28] G. EW: 'Heat Transfer and Penetration Mechanisms with GMA and Plasma-GMA Welding', *Weld. J.*, 1981, 60:37-42.
[29] Y. LI, Z. YUN, W. ZHANG, X. LONG, J. ZHU: '3D Modelling of Layer-by-Layer Heat and Mass Transfer in Wire Arc Additive Manufacturing', *Addit. Manuf. Front.*, 2024, 3:200159.

[30] M. SZILVÁSI-NAGY, G. MÁTYÁSI: 'Analysis of STL files', *Math. Comput. Model.*, 2003, 38:945-60.
[31] L. ZHOU, J. LI, G. LIN: 'Implementation of arbitrary polyhedral elements for automatic dynamic analyses of three-dimensional structures', *Sci. Rep.*, 2022, 12:4156.
[32] A. RAMOS, J. A. SIMÕES: 'Tetrahedral versus hexahedral finite elements in numerical modelling of the proximal femur', *Med. Eng. Phys.*, 2006, 28:916-24.
[33] J. SUN, J. HENSEL, M. KÖHLER, K. DILGER: 'Residual stress in wire and arc additively manufactured aluminum components', *J. Manuf. Process.*, 2021, 65:97-111.
[34] S. ROUQUETTE, C. CAMBON, I. BENDAOUD, S. CABEZA, F. SOULIÉ: 'Effect of Layer Addition on Residual Stresses of Wire Arc Additive Manufactured Stainless Steel Specimens', *J. Manuf. Sci. Eng.*, 2024, 146.
[35] SIMUFACT ENGINEERING COMPANY: *Theory and user information*, Germany, 2016.
[36] R. F. V. SAMPAIO, J. P. M. PRAGANA, I. M. F. BRAGANÇA, C. M. A. SILVA, C. V. NIELSEN, P. A. F. MARTINS: 'Modelling of wire-arc additive manufacturing – A review', *Adv. Ind. Manuf. Eng.*, 2023, 6:100121.
[37] H. ZHAO, G. ZHANG, Z. YIN, L. WU: 'Three-dimensional finite element analysis of thermal stress in single-pass multi-layer weld-based rapid prototyping', *J. Mater. Process. Technol.*, 2012, 212:276-85.
[38] Y. LI, W. GAN, W. ZHOU, D. LI: 'Review on residual stress and its effects on manufacturing of aluminium alloy structural panels with typical multi-processes', *Chinese J. Aeronaut.*, 2023, 36:96-124.
[39] J. SUN, T. NITSCHKE-PAGEL, K. DILGER: 'Generation and distribution mechanism of welding-induced residual stresses', *J. Mater. Res. Technol.*, 2023, 27:3936-54.
[40] J. CHEON, S. J. NA: 'Prediction of welding residual stress with real-time phase transformation by CFD thermal analysis', *Int. J. Mech. Sci.*, 2017, 131-132:37-51.
[41] S. BEHSERESHT, Y. H. PARK: 'Warpage Prediction in Wire Arc Additive Manufacturing: A Comparative Study of Isotropic and Johnson–Cook Plasticity Models', *Metals (Basel)*, 2025, 15.
[42] C. S. KIM: *Thermophysical properties of stainless steels*, United States: 1975.
[43] Z. CHEN, L. YUAN, Z. PAN, H. ZHU, N. MA, D. DING, H. LI: 'A comprehensive review and future perspectives of simulation approaches in wire arc additive manufacturing (WAAM)', *Int. J. Extrem. Manuf.*, 2025, 7:22016.
[44] Y. H. KIM, D. R. GUNASEGARAM, P. W. CLEARY, A. B. MURPHY: 'Numerical modelling of wire arc additive manufacturing: methods, status, trends, and opportunities', *J. Phys. D. Appl. Phys.*, 2025, 58:143001.
[45] P. K. DILJITH, P. K. CHAURASIA, B. K. BARIK, A. DE: 'Numerical modelling of gas metal arc directed energy deposition induced residual stress and distortion', *Weld. Int.*, n.d.:1-11.
[46] Y. S. TOULOUKIAN, R. W. POWELL, C. Y. HO, M. C. NICOLAOU: 'Thermophysical Properties of Matter – The TPRC Data Series, Vol. 10: Thermal Diffusivity', *IFI/Plenum*, 1973.